# HHS Public Access

# Characterizing Prostate Tumor Mouse Xenografts with CEST and MT-MRI and Redox Scanning

**Kejia Cai**, **He N. Xu**, **Anup Singh**, **Mohammad Haris**, **Ravinder Reddy**, and **Lin Z. Li**

Department of Radiology, University of Pennsylvania, 250 Anatomy Chemistry, Philadelphia, PA 19014, USA

## Abstract

The main goal of this study was to use multimodality imaging methods to reveal the heterogeneity in prostate cancer and seek the correlation between the characteristic heterogeneity and tumor aggressiveness. Here we report the preliminary data on chemical exchange saturation transfer (CEST) and magnetization transfer (MT) magnetic resonance imaging (MRI) and redox scanning [cryogenic NADH/Fp (reduced nicotinamide adenine dinucleotide/oxidized flavoproteins) fluorescence imaging] of two aggressive human prostate tumor lines (DU-145 and PC-3) xenografted in athymic nude mice. The results obtained by these methods appeared to be consistent, with all showing a higher level of heterogeneity in DU-145 tumors than in PC-3 tumors. DU-145 tumors showed CEST maps with both positive and negative areas while PC-3 CEST maps were relatively homogeneous. The mean CEST value for PC-3, $23.0 \pm 2.1$ %, is at a significantly higher level ($p < 0.05$) than DU-145 ($1.9 \pm 6.7$ %) at the peak of the CEST asymmetric curve (+2 ppm). Fp redox ratio (Fp/(NADH + Fp)) images exhibited localized highly oxidized regions in DU-145 tumors, whereas PC-3 tumors appeared to be less heterogeneous. These results suggest a possible role of metabolism in tumor progression. More studies, including an indolent prostate tumor line and with larger sample size, will be performed in the future to identify the biomarkers for prostate tumor aggressiveness.

### Keywords

Mitochondrial redox state; Fluorescence imaging; Metabolism; Tumor aggressiveness

## 1 Introduction

Prostate cancer tops the most common cancers and is the second leading cause of cancer death in males in the USA (Center for Disease Control and Prevention http://www.cdc.gov/cancer/dcpc/data/men.htm). Globally, the highest incidence rates were recorded primarily in the developed countries of Oceania, Europe, and North America in 2008 [1]. Metastasis is the primary cause of death of prostate cancer patients. Predicting prostate tumor aggressiveness (metastatic potential) to assist treatment strategies is of major importance. Our ultimate goal for this study was to identify effective metabolic/functional imaging

Correspondence to: Lin Z. Li.

Kejia Cai and He N. Xu contributed equally.

biomarkers for the prediction of prostate tumor metastatic potential. Previously, we showed that multimodality imaging methods (NMR and optical) are beneficial in predicting tumor aggressiveness in five lines of human melanoma xenografts spanning a full range of metastatic potential [2, 3]. In this paper, we report the preliminary data on the characterization of prostate tumor xenografts using chemical exchange saturation transfer (CEST) and magnetization transfer (MT) magnetic resonance imaging (MRI) and the redox scanning methods.

Conventional MT-MRI provides a unique contrast associated to bound water protons [4, 5]. After saturating macromolecular bound protons with off-resonance radio frequency pulses, the macromolecular proton spins transfer saturation to the bulk water, creating the MRI-detectable signal change from the bulk water. CEST-MRI that utilizes proton chemical exchange effects specifically from –OH, –NH, and $-NH_2$ groups of metabolites has been recently explored to map the tissue pH [6, 7], glycosaminglycans in cartilage [8], as well as liver glycogen [9]. The redox scanning of snap-frozen tissue [10, 11] gives the in vivo mitochondrial redox state by imaging the intrinsic fluorescences of NADH and Fp including FAD (flavin adenine dinucleotide), providing sensitive indicators of tumor mitochondrial metabolic states as shown in our previous studies [2, 3, 12, 13].

## 2 Methods

Two classical cell lines of human prostate cancer, PC-3 and DU-145, were chosen for the initial experiments, which have high and moderate invasive potential, respectively [14]. All animal experiments were performed according to a protocol approved by the University of Pennsylvania Institutional Animal Care and Use Committee (IACUC). The propagated cells were implanted subcutaneously into the upper thighs of athymic nude mice (~7 million cells/site).

Mice bearing DU-145 ($n = 3$) and PC-3 ($n = 4$) prostate tumors (5 weeks growth period) were under anesthesia using isofluorane and scanned at a Varian 9.4-T horizontal MRI scanner. CEST Z-spectra were collected from tumor central cross sections using a custom-programmed sequence, with a frequency selective rectangle saturation pulse ($B_1 = 250$ Hz, 1 s), followed by a segmented RF spoiled gradient echo readout. Sequence parameters were: field of view $35 \times 35$ mm$^2$, slice thickness 2 mm, flip angle 15°, readout TR 6.2 ms, TE 2.9 ms, matrix size $128 \times 128$, and number of averages 2. One saturation pulse followed with 64 segment acquisition was repeated every 4 s. Saturation frequency was arrayed from −5 to 5 ppm (part per million with respect to the water resonance) with 0.25 ppm step size. In addition, images with saturation at ±10, ±20, and ±100 ppm were acquired. MT "on" and "off" images are images with +20 and +100 ppm saturation offsets, respectively. Saturation with +100 ppm preserves over 99 % of signal based on our observation. $B_0$ and $B_1$ maps were generated for correction CEST contrast [15].

For redox scanning, mice under anesthesia underwent snap-freezing procedures and tumors were harvested and embedded as previously reported [13, 16, 17]. Redox scanning of four DU-145 and three PC-3 tumors was performed at various tissue depths. The nominal concentrations of tissue NADH and Fp were calibrated to corresponding reference standards.

All image processing and data analysis was performed using Matlab. Z-spectrum was plotted as the percentage of saturated signal (averaged within tumor regions and across all tumors in each line) as a function of saturation offset in ppm. The MTR asymmetric curve or the CEST contrast as a function of saturation offset was generated by subtracting the reference signal at the negative side of the Z-spectrum from their positive counterparts and then normalized by the reference signal. CEST contrast at a specific chemical shift (2 ppm) and MT ratio (MTR or $1 - MT_{\text{"on"}}/MT_{\text{"off"}}$) were also obtained on a pixel basis and then color mapped and overlaid onto the anatomical images acquired when MT was turned "on."

## 3 Results

DU-145 shows higher levels of signal compared to PC-3 across the entire Z-spectrum (Fig. 6.1a), indicating lower level of magnetization transfer effects from DU-145. The MTR asymmetric curve of PC-3 (Fig. 6.1b) shows positive CEST contrast, while contrast from DU-145 is mostly negative with large variation. DU-145 tumors showed a heterogeneous MTR and CEST distribution while PC-3 maps were relatively homogeneous (Fig. 6.2a–f). Extremely low MTR regions seen from DU-145 indicate possible tumor necrosis. Although there is no significant difference in MTR mean values (Fig. 6.2g) between DU-145 and PC-3, the mean CEST contrast (Fig. 6.2h) for PC-3 ($23.0 \pm 2.1$ %) is at a significantly higher level ($p < 0.05$) than DU-145 ($1.9 \pm 6.7$ %) at +2 ppm of chemical shift, the peak of the CEST asymmetric curve.

Figure 6.3 shows typical redox images of the two types of tumors. The distinct heterogeneity in the Fp, NADH, and Fp redox ratio (Fp/(NADH + Fp)) images was clearly seen in all four tumors of DU-145, whereas two out of three PC-3 tumors appeared to be less heterogeneous. The global averages of Fp, NADH, and Fp redox ratio for DU-145 (4 tumors, 15 sections scanned) are $582 \pm 196$ μM, $390 \pm 140$ μM, and $0.59 \pm 0.09$, respectively; whereas those for PC-3 (3 tumors, 11 sections scanned) are $553 \pm 303$ μM, $350 \pm 170$ μM, and $0.58 \pm 0.11$, respectively. These values obtained by averaging the mean from each tissue section of the same type of tumor are not significantly different between the two lines.

The results obtained by the three imaging methods appeared to be consistent, with all showing a higher level of heterogeneity in the DU-145 tumors than that in the PC-3 tumors.

## 4 Discussion and Conclusion

MTR contrast originates from bound water protons that are associated with relatively stationary structural tissue proteins and lipids. The typical exchange rate for these bound protons is less than 20 Hz, while the CEST effect of macromolecule, peptides, and free amino acids is due to exchangeable protons with an exchange rate ($k$) from 10 to several kHz [18, 19]. In order to observe the CEST effect, $k$ should be within a slow to intermediate regime compared to the chemical shift ($\omega$), i.e., under the condition of $k$ $\omega$. Additionally, at any given saturation amplitude, a maximum CEST effect is observed when $k \sim 2\pi B_1$ in Hz [20]. That is why saturation with $B_1$ as low as 50 Hz has been used for CEST imaging of amide proton transfer (APT) with $k \sim 30$ Hz [7]. Using higher $B_1$ decreases CEST contribution from APT and activates small molecule metabolites and mobile peptides.

In this study, CEST contrast created by using 250 Hz $B_1$ may be mostly due to free amino acids with an exchange rate of ~1.5 kHz (or $2\pi \times 250$ Hz). CEST contrast could be used to reflect tissue metabolism involving free amino acids (such as alanine and glycine) and other organic molecule (such as creatine). Further investigation is needed to find the specific small molecule metabolites that contribute to CEST-MRI contrast in prostate cancers.

Our previous quantitative studies on the metastatic potential of melanoma [2, 3] and breast tumor [13] xenografts indicated that a high level of heterogeneity in mitochondrial redox state is associated with tumor aggression, and the aggressive tumors have localized highly oxidized regions while the indolent ones are usually more homogeneous and do not have localized oxidized regions. Although we have not found data showing direct measurement of the metastatic potential of these two lines in vivo, published data suggest that the DU-145 line is less invasive than PC-3 in vitro [14, 21]. The observed heterogeneity in the MRI and redox state imaging results seems to support that the intra-tumor heterogeneity of the DU-145 tumors was more distinct than that of PC-3 tumors. These results prompt further examination to elucidate whether such heterogeneity difference is due to the intrinsic difference in cancer biology. Global average of the redox indices in this study shows no significant difference between the two prostate tumor lines, suggesting that more specific analysis on redox state of tumor heterogeneity is required, which will be conducted in the near future.

More studies including an indolent prostate tumor line (such as LnCap) and with larger sample size will be carried out to identify the molecular imaging biomarkers for prostate tumor aggressiveness. We would also be interested in measuring tissue oxygenation to know whether these tumors were under acute or chronic hypoxia which, according to a recent in vitro study [22], may increase the invasiveness or cause cell death. Histological staining of vasculatures, cell death, or hypoxia (HIF) may help us to gain more understanding of our observations from the MRI and the redox scanning.

As a conclusion, CEST- and MT-MRI and redox scanning were successfully employed to reveal the heterogeneity in prostate tumor xenografts. Data showed more heterogeneity in the DU-145 than in the PC-3 xenografts. The CEST and MT-MRI are non-invasive and potentially translatable to the clinic while the redox scanning can be applied to the biopsy specimen.

## Acknowledgments

## References

1. Jemal A, Bray F, Center MM, et al. Global cancer statistics. CA Cancer J Clin. 2011; 61:69. [PubMed: 21296855]

2. Li LZ, Zhou R, Xu HN, et al. Quantitative magnetic resonance and optical imaging biomarkers of melanoma metastatic potential. Proc Natl Acad Sci U S A. 2009; 106:6608–6613. [PubMed: 19366661]

3. Li LZ, Zhou R, Zhong T, et al. Predicting melanoma metastatic potential by optical and magnetic resonance imaging. Adv Exp Med Biol. 2007; 599:67–78. [PubMed: 17727249]

4. Grossman RI, Gomori JM, Ramer KN, et al. Magnetization transfer: theory and clinical applications in neuroradiology. Radiographics. 1994; 14:279–290. [PubMed: 8190954]

5. Henkelman RM, Stanisz GJ, Graham SJ. Magnetization transfer in MRI: a review. NMR Biomed. 2001; 14:57–64. [PubMed: 11320533]

6. Sun PZ, Zhou J, Sun W, et al. Detection of the ischemic penumbra using pH-weighted MRI. J Cereb Blood Flow Metab. 2006; 27:1129. [PubMed: 17133226]

7. Zhou J, Payen JF, Wilson DA, et al. Using the amide proton signals of intracellular proteins and peptides to detect pH effects in MRI. Nat Med. 2003; 9:1085–1090. [PubMed: 12872167]

8. Ling W, Regatte RR, Navon G, et al. Assessment of glycosaminoglycan concentration in vivo by chemical exchange-dependent saturation transfer (gagCEST). Proc Natl Acad Sci U S A. 2008; 105:2266–2270. [PubMed: 18268341]

9. van Zijl PCM, Jones CK, Ren J, et al. MRI detection of glycogen in vivo by using chemical exchange saturation transfer imaging (glycoCEST). Proc Natl Acad Sci. 2007; 104:4359–4364. [PubMed: 17360529]

10. Chance B, Schoener B, Oshino R, et al. Oxidation–reduction ratio studies of mitochondria in freeze-trapped samples. NADH and flavoprotein fluorescence signals. J Biol Chem. 1979; 254:4764–4771. [PubMed: 220260]

11. Quistorff B, Haselgrove JC, Chance B. High spatial resolution readout of 3-D metabolic organ structure: An automated, low-temperature redox ratio-scanning instrument. Anal Biochem. 1985; 148:389–400. [PubMed: 4061818]

12. Xu HN, Nioka S, Chance B, et al. Heterogeneity of mitochondrial redox state in premalignant pancreas in a PTEN null transgenic mouse model. Adv Exp Med Biol. 2011; 201:207–213.

13. Xu HN, Nioka S, Glickson JD, et al. Quantitative mitochondrial redox imaging of breast cancer metastatic potential. J Biomed Opt. 2010; 15:036010. [PubMed: 20615012]

14. Pulukuri SM, Gondi CS, Lakka SS, et al. RNA interference-directed knockdown of urokinase plasminogen activator and urokinase plasminogen activator receptor inhibits prostate cancer cell invasion, survival, and tumorigenicity in vivo. J Biol Chem. 2005; 280:36529–36540. [PubMed: 16127174]

15. Haris M, Cai K, Singh A, et al. In vivo mapping of brain myo-inositol. Neuroimage. 2010; 54:2079–2085. [PubMed: 20951217]

16. Xu HN, Wu B, Nioka S, et al. Calibration of redox scanning for tissue samples. Proc SPIE. 2009; 7174:71742F1–71742F8.

17. Xu HN, Wu B, Nioka S, et al. Quantitative redox scanning of tissue samples using a calibration procedure. J Innov Opt Health Sci. 2009; 2:375–385.

18. van Zijl PCM, Zhou J, Mori N, et al. Mechanism of magnetization transfer during onresonance water saturation. A new approach to detect mobile proteins, peptides, and lipids. Magn Reson Med. 2003; 49:440. [PubMed: 12594746]

19. van Zijl PCM, Yadav NN. Chemical exchange saturation transfer (CEST): what is in a name and what isn't? Magn Reson Med. 2011; 65:927. [PubMed: 21337419]

20. Woessner DE, Zhang S, Merritt ME, et al. Numerical solution of the Bloch equations provides insights into the optimum design of PARACEST agents for MRI. Magn Reson Med. 2005; 53:790–799. [PubMed: 15799055]

21. Laniado ME, Lalani EN, Fraser SP, et al. Expression and functional analysis of voltage-activated Na+ channels in human prostate cancer cell lines and their contribution to invasion in vitro. Am J Pathol. 1997; 150:1213–1221. [PubMed: 9094978]

22. Dai Y, Bae K, Siemann DW. Impact of hypoxia on the metastatic potential of human prostate cancer cells. Int J Radiat Oncol. 2011; 81:521–528.
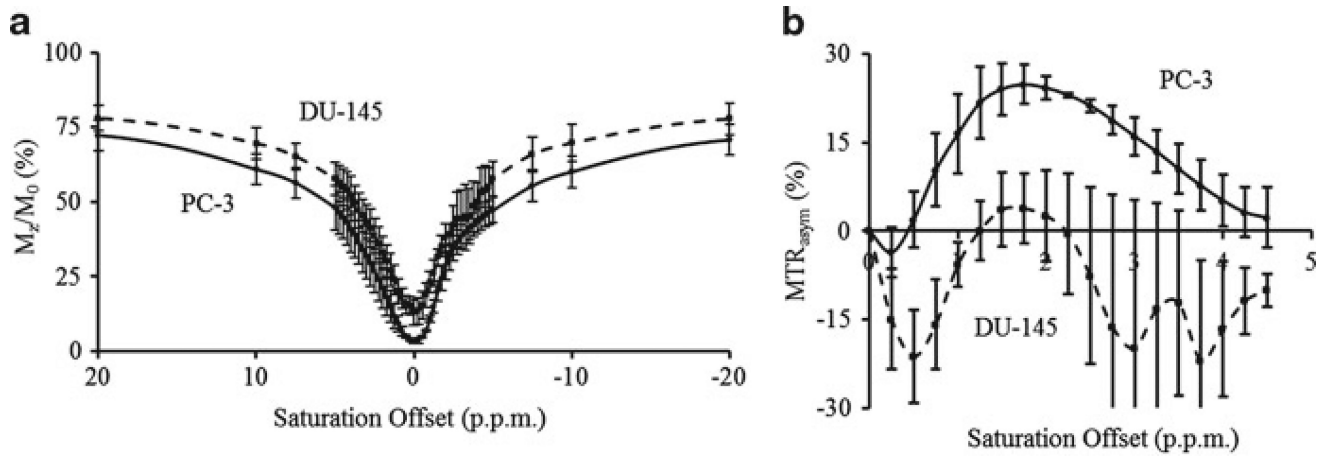
**Fig. 6.1.**
Z-spectra (**a**) and MTR asymmetric curves (**b**) of DU-145 (*dashed*) and PC-3 (*solid*) prostate tumors. Data are averaged within tumor regions and across all tumors for each tumor line
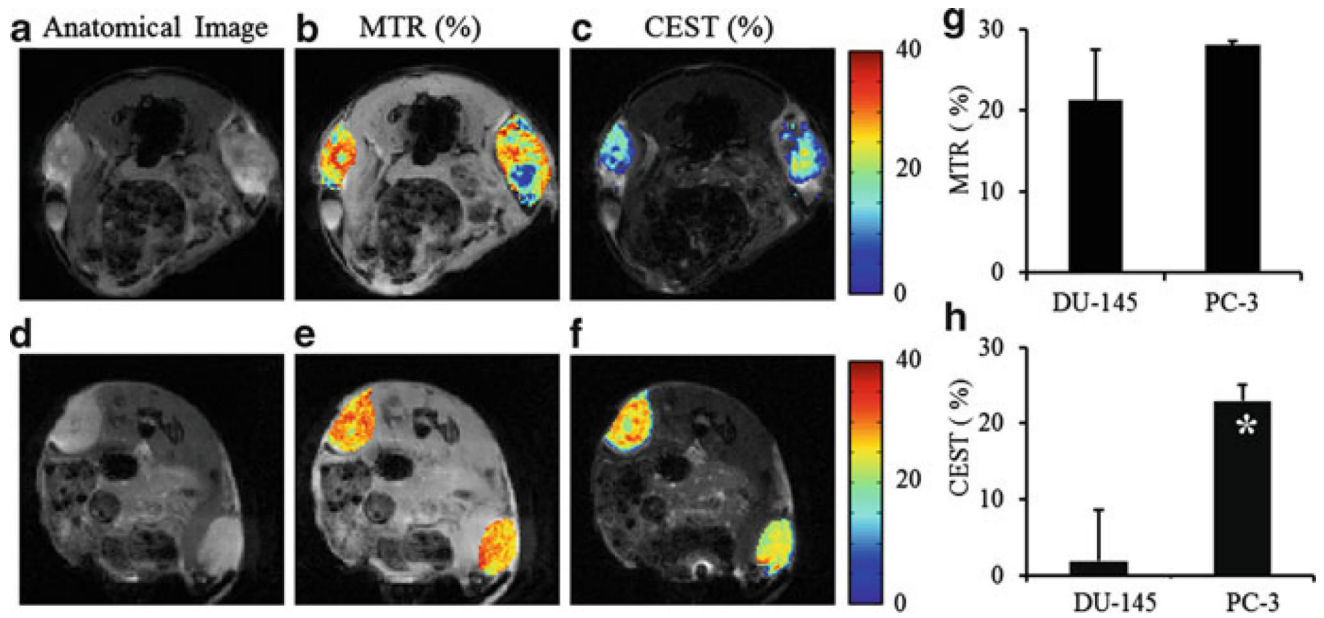
**Fig. 6.2.**

Anatomy images (**a, d**), +20 ppm MTR (**b, e**), and +2 ppm CEST (**c, f**) maps of a typical DU-145 tumor (*top*) and a typical PC-3 tumor (*bottom*). CEST contrast of PC-3 ($n = 4$) is significantly higher than DU-145 ($n = 3$) (**h,** $p < 0.05$), while their MTR contrasts are similar (**g,** $p > 0.05$)
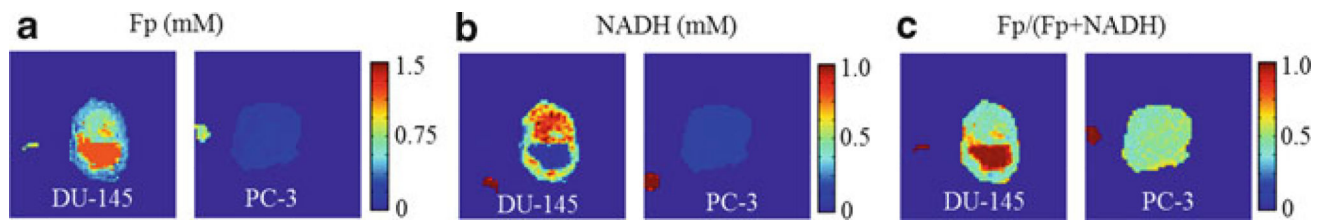
**Fig. 6.3.**
Typical redox images (Fp, NADH, and Fp redox ratio) of DU-145 and PC-3 xenografts. The *small round spots* outside the tumors are the reference standards